High-Density 2D Homo- and Hetero- Plasmonic Dimers with Universal Sub-10-nm Gaps

Mingliang Zhang,[†,⊥] Nicolas Large,[∥,¶] Ai Leen Koh,[§] Yang Cao,[∥] Alejandro Manjavacas,[∥] Robert Sinclair,[†] Peter Nordlander,[*,∥] and Shan X. Wang[*,†,‡]

[†]Materials Science and Engineering, [‡]Electrical Engineering, and [§]Stanford Nano Shared Facilities, Stanford University, Stanford, California, United States and [∥]Department of Physics and Astronomy, Laboratory for Nanophotonics, Rice University, Houston, Texas, United States. [⊥]Present address: Department of Electrical and System Engineering, University of Pennsylvania, Philadelphia, Pennsylvania, United States. [¶]Present address: Department of Chemistry, Northwestern University, Evanston, Illinois, United States.

ABSTRACT Fabrication of high-density plasmonic dimers on a large (wafer) scale is crucial for applications in surface-enhanced spectroscopy, bio- and molecular sensing, and optoelectronics. Here, we present an experimental approach based on nanoimprint lithography and shadow evaporation that allows for the fabrication of high-density, large-scale homo- (Au—Au and Ag—Ag) and hetero- (Au—Ag) dimer substrates with precise and consistent sub-10-nm gaps. We performed scanning electron, scanning transmission electron, and atomic force microscopy studies along with a complete electron energy-loss spectroscopy (EELS) characterization. We observed distinct plasmonic modes on these dimers, which are well interpreted by finite-difference time-domain (FDTD) and plasmon hybridization calculations.

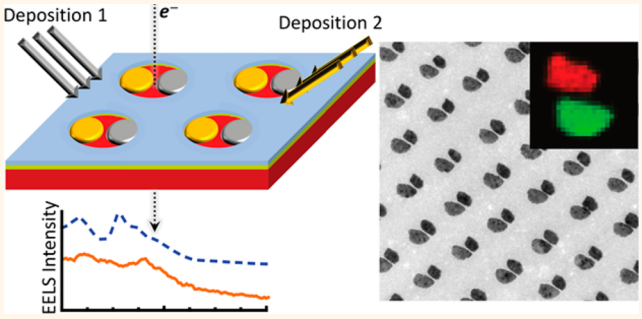

KEYWORDS: plasmonic dimers · nanoimprint lithography · shadow evaporation · electron energy-loss spectroscopy (EELS) · finite-difference time-domain (FDTD) · plasmon hybridization

The plasmonic properties of noble metal nanostructures have been widely studied and pursued in various applications ranging from molecular sensing[1−3] to light manipulation.[4−7] Since the optical properties of plasmonic systems are closely related to the morphology of the nanostructures, there is a strong need for the development of fabrication methods that provide precise geometrical control and at the same time have high-throughput yields. Among the large variety of plasmonic nanostructures, dimers have received particular interest, as they are able to confine and localize the electromagnetic field down to the nanoscale and provide near-field enhancements by several orders of magnitude, leading to the formation of plasmonic hot-spots.[8,9] These hot-spots are of high interest in a wide range of applications such as surface-enhanced spectroscopies,[3,10−12] bio- and molecular sensing,[13,14] optoelectronics,[15] and plexcitonics.[12,16,17] The plasmonic dimer geometry is also often adopted as a model system for studying plasmonic interactions and how these can be employed for tuning the near and far-field.[18] Chemical syntheses, such as seed-mediated growth[19] and induced aggregation,[20,21] have been explored to fabricate dimer structures due to their high-throughput capacity, but the former can yield only dimers with a conductive junction, and the latter typically suffers from poor control over the sizes of the aggregations. Electron-beam lithography (EBL),[18,22] electron-beam manipulation,[23] and He^+-ion lithography[24] have proven to be very efficient for making small-scale few-dimer substrates, yet they are not suitable for wafer-scale production. Angle-resolved nanosphere lithography[25,26] and stencil lithography[27] can make large-scale dimer structures, yet it is not trivial to reach a sub-10-nm gap size.

Here, using a combination of nanoimprinting lithography (NIL)[28−31] and shadow evaporation,[32] we report a new method for producing

* Address correspondence to nordland@rice.edu (P. Nordlander); sxwang@stanford.edu (S. X. Wang).

Received for review May 21, 2015 and accepted July 22, 2015.

Published online July 22, 2015
10.1021/acsnano.5b03090

wafer-scale, high-density Au−Au and Ag−Ag dimer arrays with uniform size, well-defined orientation, and controllable gap morphology. Protocols have been adapted to be able to achieve sub-10-nm gap configurations. This facile technique also allows, with minor adjustments, the fabrication of heterodimers, in which each particle in the dimer is made of a different metal (*e.g.*, Au−Ag dimers). Meanwhile, protocols have been established to pattern dimer nanostructures on a 50 nm thin Si_3N_4 membrane, which allows us to use scanning transmission electron microscopy (STEM) and perform electron energy-loss spectroscopy (EELS) on individual dimers. Here we present EELS measurements on Ag−Ag, Au−Au, and Au−Ag dimers with sub-10-nm gaps. We complement these measurements with EELS calculations carried out using the finite-difference time-domain (FDTD) method, which, together with a plasmon hybridization (PH) model,[33,34] allows a deeper understanding of the experimental results and provides a qualitative picture of the plasmonic modes involved in these strongly coupled dimers.

RESULTS AND DISCUSSION

The dimer patterning procedure is illustrated in Figure 1. Dimers are patterned on either Si or Si_3N_4 substrates. In step 1, two layers of resist, poly(methyl glutarimide) (PMGI) and poly(methyl methacrylate) (PMMA), are sequentially spin-coated onto the substrate. Then (step 2), the top PMMA layer is nano imprinted with a self-assembled template patterned with pillar array to generate a hole pattern. In the current setup, the pillars are fabricated using nanosphere lithography[29] and have a diameter of 150 nm and a pitch size of 390 nm. In step 3, the substrate is reactive-ion etched to remove the residual PMMA in the hole and wet-etched to partially dissolve the PMGI layer through the holes, forming an undercut structure. Shadow evaporation occurs in steps 4 and 5, noted as first-run and second-run deposition, respectively. Contrary to the usual normal incidence deposition, noble metals are here evaporated into the holes at oblique incidences. The deposition angles α (first run) and β (second run) are adjusted such that each part of the dimer takes half of the bottom of the hole. The control over the deposition angles determines the nanoparticle spacing (*i.e.*, gap size). The residual metallic sheet atop the PMMA layer is then removed by lift-off (step 6). The detailed process is described in the Methods section.

Figure 2A shows a scanning electron microscopy (SEM) image of Ag−Ag dimers forming hexagonal patterns all over the surface. Because the metal deposition direction is universal, all the dimers are aligned along the same direction. As it can be seen from Figure 2B,C, the dimers consist of two disk-like nanoparticles separated by a gap. Due to the evaporation process, the gaps are elongated and perpendicular to

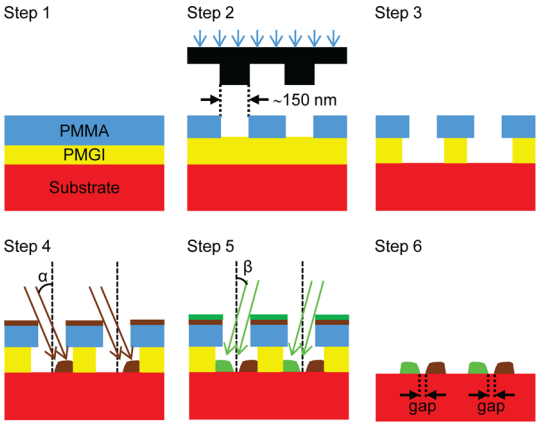

Figure 1. Schematic of dimer array fabrication. Step 1: resist spin-coating. Step 2: nanoimprinting with a pillar-patterned template. Step 3: dry-etching and wet-etching to form undercut structures. Step 4: first-run angular e-beam evaporation of metal with an angle α with respect to the wafer normal. Step 5: second-run angular deposition of metal with an angle β with respect to the wafer normal, having a 180° azimuthal angle with respect to the first-run deposition. Step 6: lift-off to expose the dimer array on the substrate.

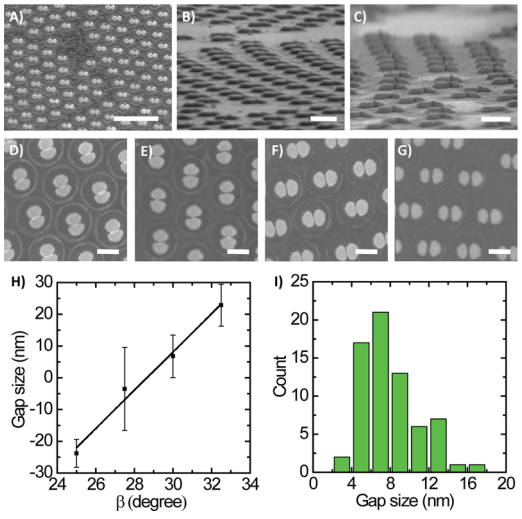

Figure 2. As-fabricated dimer structure. (A) SEM image of a plane-view Ag−Ag dimer array on a Si substrate before PMGI removal (scale bar: 1 μm). (B, C) SEM images of a side-view Ag−Ag dimer array on a Si substrate (scale bar: 200 nm). (D−G) SEM images of a plane-view Ag−Ag dimer array on a Si_3N_4 substrate with a fixed first-run deposition angle α = 35° and different second-run deposition angle β of (D) 25°, (E) 27.5°, (F) 30°, and (G) 32.5° (scale bar: 200 nm). (H) Relationship between the gap size and the deposition angle β. (I) Gap size distribution of Ag−Ag dimers with wafer-scale inspection of 70 dimers.

the dimer axes. Since the gap sizes are approaching the SEM spatial resolution, they can barely be identified. The gap structure can be characterized in a more detailed manner using transmission electron microscopy (TEM) and atomic force microscopy (AFM), as we will discuss later.

The deposition angles, α and β, are crucial for obtaining the desired dimer structure, as the process is purely geometrical.[25] Larger deposition angles lead

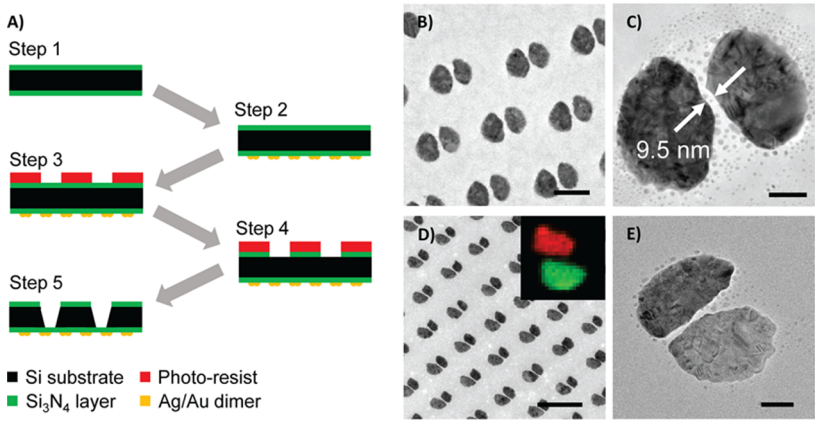

Figure 3. Fabricating a dimer array TEM sample. (A) Fabrication schematic: step 1, nitride coating onto both sides of a Si wafer; step 2, patterning of the dimer array structure on one side of the wafer; step 3, patterning of a square TEM observation window on the photoresist on the other side of the wafer; step 4, dry-etching through the nitride layer; step 5, KOH etching through the Si layer to expose the bottom nitride window. (B) Au−Au dimer array on a Si_3N_4 membrane (scale bar: 200 nm) under a bright-field TEM image. (C) Zoomed-in image of one Au−Au dimer with a sub-10-nm gap (scale bar: 50 nm). (D) Au−Ag heterodimer array (scale bar: 500 nm). Inset shows elemental mapping of one dimer, with red representing Au and green representing Ag. (E) Zoomed-in image of one Au−Ag dimer with a sub-10-nm gap (scale bar: 50 nm).

to the displacement of the dimer further away from the center of the deposition hole and narrower nanoparticles (*i.e.*, more elliptical). When α and β have similar values, the deposition process leads to asymmetrical dimer structures. The reason is that the deposited materials on the side wall of the PMMA during the first run will play the role of an additional, undesired, masking layer during the second-run deposition (Figure S1, Supporting Information). To avoid this undesired effect, a smaller value of β (compared with α) is necessary to obtain a dimer with two nanoparticles of similar sizes. As shown in the SEM images, by increasing β (keeping α constant), the dimers change from partially overlapping (Figure 2D,E) to well separated (Figure 2F,G). AFM images are shown in Figure S2 of the Supporting Information. Figure 2H shows the statistical measurement of the average gap size as a function of the deposition angle β, while α is kept at a fixed value of 35°. It is revealed that a 1° increase of β leads to a 4.5 nm increase of the average gap size. Importantly, the gap sizes are sampled over a centimeter-sized area. Across the entire area, a simple geometrical calculation revealed that the gap size variation caused by the difference in deposition angle as a result of shadow evaporation is only 1.1 nm under the current deposition configuration (Figure S3, Supporting Information). Even considering the full-wafer fabrication (*i.e.*, 4 × 4 cm^2 nanoimprint template), the corresponding size variation is 4.5 nm. To further demonstrate the wafer-scale control of the gap sizes, dimers were fabricated in a square area of 4 × 4 cm^2, and gap sizes were surveyed from center to edge. The gap size distribution of a given optimized process, shown in Figure 2I, shows an average gap distance of 7.7 nm and a standard deviation of 3.1 nm. Consequently, by tuning the deposition angle, sub-10-nm gaps can be consistently generated over wafer scale. The negative values of the gap distance for $\beta \leq 28°$ stand for the cases when dimers are in an overlapping configuration, and their absolute values represent the width of the overlapping region. Since the generation of the dimer structure is purely geometrical, the thickness of PMGI and PMMA layers and the diameter of the holes will also directly affect the dimer geometry. Therefore, a careful optimization should be performed for each distinct situation to obtain the desired nanostructure.

The dimer density, *i.e.*, the number of dimers that can be fabricated per surface area, is determined by the pillar structure on the template. Here, using a template with pillars of 390 nm pitch size, the fabricated dimers have a surface density of 8 dimers/μm^2. Notably, templates with pillars of 200 nm pitch size have also been reported,[29] which can potentially reach a higher dimer density. This value can be further increased by using a more advanced technique to pattern templates, such as block copolymer self-assembly.[35] Using this technique holes with a 28.6 nm pitch size have been already patterned.[36] If dimers were fabricated using a similar template, one could expect a surface density of ~1500 dimers/μm^2. However, such high dimer densities may not always be desirable depending on the targeted application. When the dimers are brought in close proximity to each other, dimer−dimer interactions can occur and strongly influence the optical properties of the patterned substrates (*e.g.,* localized surface plasmon resonance (LSPR) shift and hot-spot alteration).

To better visualize and spatially resolve nanoscale geometrical features, we perform TEM imaging of these dimers by placing the plasmonic dimers onto a 50 nm thin Si_3N_4 substrate. As shown in Figure 3A, a double-sided polished Si (100) wafer is coated on both sides with a thin Si_3N_4 membrane first (step 1), followed by the patterning of a plasmonic dimer array

on one side according to the protocol described earlier (step 2). The silicon nitride membrane on the other side is subsequently patterned to have 0.5 × 0.5 mm^2 open windows where the underneath Si is exposed (steps 3 and 4). KOH etching is then used to etch through the Si wafer in the window area to expose the nitride layer with the dimer array structure atop (step 5). The final Si_3N_4 membrane has a length of 0.2 mm, smaller than the initial patterned region, as a result of KOH anisotropic etching (Figure S4, Supporting Information). Detailed fabrication information can be found in the Methods section.

Figure 3B shows a TEM bright-field image of a typical Au−Au dimer array supported by a thin silicon nitride membrane. Essentially, the dimer structure is the same as the sample fabricated on the Si wafer. The gap structure is more clearly resolved owing to the subnanometer resolving power of the instrument. From the TEM images, we demonstrate that sub-10-nm gaps can be consistently fabricated (Figure 3C and Figure S5, Supporting Information). One can notice the presence of subnanometer metallic particles surrounding the dimers, possibly resulting from the lift-off process. FDTD simulations have shown that these particles have negligible effects on the overall plasmonic properties of the dimers (data not shown here). Although the fabricated dimer structures are not perfect compared with those patterned by e-beam lithography, the fabrication efficiency is orders-of-magnitude higher. There is a trade-off between precise shape control and large-scale production.

The flexibility of our fabrication method also allows for fabricating heterodimers with nanometer-sized gaps. As shown in Figure 3D, Au−Ag heterodimers are fabricated on the entire wafer area. In the TEM bright-field image, the Au nanoparticle appears darker than the Ag nanoparticle due to the difference in atomic numbers *Z*. Indeed, such a color contrast cannot be caused by the difference of either the metal thickness or diffraction plane, as both components of the dimer are designed to have the same thickness and are both polycrystalline. Additionally, elemental mapping (inset of Figure 3D) confirms that the dimers consist of one Ag and one Au nanoparticle. Similarly to the homodimers the gap can be controlled within 10 nm by adjusting the deposition angles (Figure 3E).

EELS has been extensively used in the past few years to investigate the plasmonic properties of single metallic nanostructures,[37,38] and in particular of small nanoparticle dimers and clusters.[18,22,39−41] Here, we performed EELS measurements on the sub-10-nm-gap Au−Au and Ag−Ag dimers (Figure 4). EELS spectra are acquired with an acceleration voltage of 300 kV and with the electron beam incident on the edge of the dimer (Figure 4A,C) and at the center of the gap (Figure 4B,D). The electron beam impact is indicated as a red spot in the high-angle annular dark-field (HAADF) images in

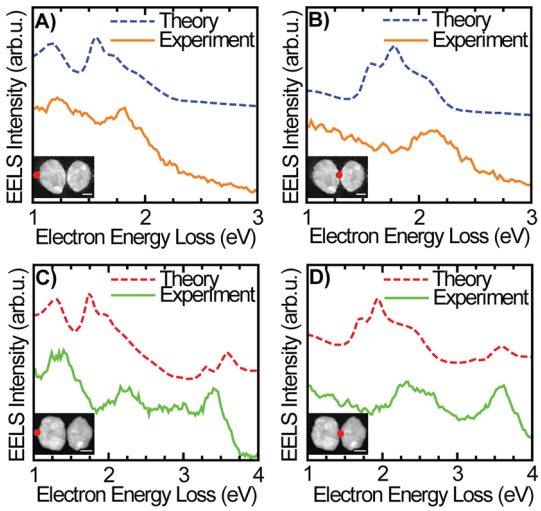

Figure 4. EELS spectra of Au−Au and Ag−Ag dimers. (A, B) EELS of a Au−Au dimer with the electron beam directed on (A) the edge part (*i.e.*, end) and (B) the center part (*i.e.*, gap) of the dimer. The orange solid lines represent the experimental data, and the blue dashed lines represent the theoretical results. (C, D) EELS of a Ag−Ag dimer with the electron beam directed onto (C) the edge part (*i.e.*, end) and (D) the center part (*i.e.*, gap) of the dimer. The green solid lines represent the experimental data, and the red dashed lines represent the theoretical results. For all cases, the insets are the corresponding HAADF images, with the red dots indicating the position of the incident electron beam (scale bar: 50 nm).

the inset of the figure panels. The zero-loss peak (Figure S6, Supporting Information) has been subtracted from each EELS spectrum using the reflected tail model. The measurement of the full-width at half-maximum (fwhm) of this zero-loss peak in turn determines the spectral resolution. Here, the fwhm was found to be 0.15 eV.

Due to the relatively large dimer−dimer distance (≥100 nm), the electromagnetic interaction between two neighboring dimers is negligible. Due to the local nature of the excitation source (*i.e.*, the electron beam), it is possible to excite and probe all the plasmonic modes of a single dimer (*i.e.*, bright and dark modes) by selecting specific impact parameters. For Au−Au dimers, the EELS spectrum associated with the electron beam spotted on the edge part (Figure 4A) exhibits two peaks at 1.2−1.3 and 1.8 eV, respectively, while the spectrum for an electron impact at the center of the gap (Figure 4B) exhibits one broad peak around 2.1 eV. For Ag−Ag dimers, the edge excitation reveals three peaks at 1.3−1.4, 2.1−2.2, and 3.3−3.4 eV, and the gap center excitation allows us to detect a broad peak from 2.3 to 2.6 eV and another peak at 3.6 eV. It should be noticed that the EELS spectra were measured at both ends of the dimers and did not show significant differences, despite the slight geometrical differences between the two nanoparticles. Systematic measurements have been conducted for several dimers, proving that the peaks mentioned above are common features of the system (Figures S7 and S8, Supporting Information).

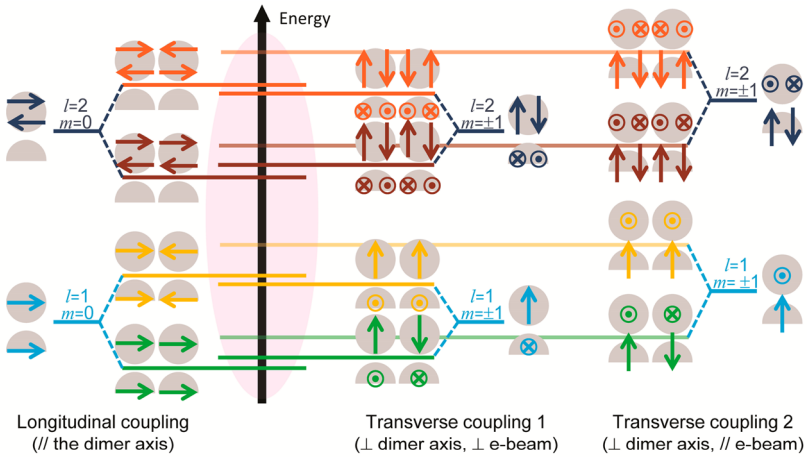

Figure 5. Schematics of the plasmon hybridization in a hemispherical dimer. In all cases, the gray disks and hemidisks are the top and side view of the nanoparticles, respectively. The arrows illustrate the electric dipoles induced by surface oscillating charges in each nanoparticle. Their colors represent different modes: green and yellow are the bonding and antibonding interactions for the dipolar (l = 1, light blue) modes, respectively; brown and orange represent the bonding and antibonding interactions for the quadrupolar (l = 2, dark blue) modes, respectively. The first column combines the hybridized modes in the longitudinal coupling configuration (*i.e.*, charge oscillations parallel to the dimer axis), while the second and third columns combine the hybridized modes in the transverse coupling configurations (*i.e.*, charge oscillations perpendicular to the dimer axis). The horizontal colored lines stand for the energy levels of the different hybridized modes. The energy levels of all the hybridized plasmon modes sustained by the dimer (longitudinal and transverse) are highlighted by the purple area.

Numerical simulations of electron-based spectroscopies have been proven to be useful in the understanding of the plasmonic properties of complex geometries.[42−45] Here, we use the FDTD method and a recently developed EELS-FDTD implementation.[45] More details on this approach can be found in the Methods section and in ref 45. On the basis of the HAADF (inset of Figure 4) data, the dimers are modeled as two hemiellipsoids supported by a silicon nitride membrane (Figure S10, Supporting Information). The maximum thickness of the dimer is 40 nm, and the gap size is fixed at 5 nm. For the Au−Au dimer, the long/short axis lengths for the two nanoparticles are 190/150 nm and 170/130 nm, respectively. For the Ag−Ag dimer, these values are set at 160/130 nm and 155/110 nm, respectively. The calculated EELS spectra are shown in Figure 4 (dashed lines). The numerical simulations are in good agreement with the experimental results and capture the salient features observed in the EELS measurements. More specifically, EELS-FDTD calculations on the Au−Au dimer reveal LSPRs around 1.2 and 1.6 eV for the edge excitation (Figure 4A) and several LSPRs between 1.6 and 2.1 eV for the gap center excitation (Figure 4B). Similarly, the calculations for the Ag−Ag dimer reveal LSPRs around 1.3, 1.8−2.1, and 3.3−3.6 eV for the edge excitation (Figure 4C) and from 1.8 to 2.2 eV and at 3.6 eV for the gap center excitation (Figure 4D). It is important to notice that the EELS-FDTD spectra for Au−Au and Ag−Ag dimers exhibit multiple smaller peaks with spectral separations approaching the experimental resolution (150 meV), which result in the broad bands observed experimentally. As the dimers are formed from elongated nanoparticles, the position of the LSPRs depends on the geometrical aspect ratios. Variations in aspect ratios across the entire sample will contribute to inhomogeneous broadening of the LSPR when collectively probed by optical spectroscopy. However, EELS is much less sensitive to this source of inhomogeneous broadening, as it probes individual nanoparticles. Other morphological details such as surface roughness, small height inhomogeneity, and deviation from the ideal semiellipsoidal geometry used in the theoretical EELS-FDTD calculations contribute to LSPR broadening and LSPR shift. Contrary to ensemble measurements, fine morphological details play a significant role in EELS measurement of individual nanostructures due to the highly localized nature of the electron beam. Local irregularities (*e.g.*, curvature, indentations) in the gap region strongly influence the local density of states in this particular region and, therefore, are reflected in the associated EELS spectrum. Moreover, such irregularities, by introducing gap size variations, directly affect the PH (*cf.* Figure S11, Supporting Information). Also, as it can be seen from the bright-field and HAADF images (*cf.* Figure 3 and Figures S5, S7, and S8, Supporting Information), tiny nanometric dots are formed around the metallic dimers. The change in surrounding environment also introduces spectral shifts of the observed LSPRs. Such morphological features can be accounted for in the EELS-FDTD calculations by introducing a very fine sub-nanometer FDTD mesh. However, we decided to keep the geometry ideally smooth, thus allowing us to investigate the physics of the system while keeping the computational cost reasonable.

Small spherical nanoparticle dimers usually exhibit a bonding and an antibonding dipolar LSPR.[22,40] However, this simple situation does not apply to the current dimer system due to its much larger particle size and lower symmetry. PH theory has been used to qualitatively account for the complexity of the EELS spectra.[33,34] Figure 5 shows a qualitative illustration of the complex plasmon hybridization in these large, symmetry-broken dimers. The gray disks and hemidisks represent the top view and side view of the dimer, respectively. The arrows represent the local dipoles induced by the surface charge oscillation associated with the plasmon modes in these two different views.

First, due to the large size of the nanoparticles (~150−200 nm), retardation effects become significant and contribute to the enhancement of higher order modes.[22,39] For the sake of simplicity, Figure 5 illustrates only the dipolar (l = 1, light blue) and quadrupolar (l = 2, dark blue) primitive modes. Second, due to the hemiellipsoidal shape, each nanoparticle of the dimer can have distinct energy levels identified by different m values ($m = 0, \pm1$) for dipolar and (m = 0, ±1, ±2) for quadrupolar modes. These azimuthal numbers, degenerated for a spherical nanoparticle, correspond to the charge oscillation along the three principle axes of the nanostructure (x-, y-, and z-directions).[38,46,47] In Figure 5, we show the m = 0 modes (first column, longitudinal coupling) and the $m = \pm1$ modes (second and third columns, transverse coupling). Third, when two particles are brought in close proximity, the hybridization between the primitive modes of each particle in the dimer causes energy level splitting, thus leading to the formation of bonding and antibonding combinations of the nanoparticle plasmons of the same multipole order l.[18,22,34,48] These bonding and antibonding hybrid modes are schematically shown in Figure 5 in yellow/green and orange/brown for l = 1 and l = 2, respectively.

Finally, the asymmetry of the dimer (*i.e.*, nanoparticles of different sizes) adds an additional level of degeneracy lifting. However, to keep the level of complexity reasonable, this effect is not shown in Figure 5. As a result of these different effects, a variety of possible energy levels appear in the energy diagram (highlighted by the purple area in Figure 5), leading to a high density of states, which are observed as broad bands in the EELS spectra (Figure 4). Under these circumstances, it is impractical to distinguish the energy level of each mode. Therefore, the peaks that appear in both experimental and theoretical spectra should be attributed to the superposition of several modes with similar energy levels. The relative intensity of each of these modes, determined by the previously discussed morphological effects, can induce apparent spectral shifts of the resulting broad bands observed in the EELS spectrum. This may result in additional discrepancies between experiment and theory. The complexity of the EELS spectra can also be observed for large dimers of spherical nanoparticles with very low gap-to-diameter ratios. A PH diagram has been calculated analytically for dimers of 160 nm Ag spheres (Figure S11, Supporting Information).[34] Even though these PH calculations do not include retardation effects, they highlight the critical role of the gap size and clearly show that, even for such a simple spherical particle case, the mode labeling becomes challenging due to the energy level crossings and anticrossings. EELS-FDTD calculations performed for such a dimer of nanospheres (a = 160 nm, g = 5 nm) clearly show the appearance of higher order LSPRs in the spectrum.[45] The fact that EELS allows to probe both dark and bright modes has been shown to be very useful for mode analysis in individual nano-objects.[18,22,23,37−40,45,47] However, the mode analysis becomes very complex in our system due to the large number of modes involved and to the strong plasmon hybridization between all these modes. In particular, the strong spectral overlap of the different modes does not allow us to properly map individual modes.

EELS spectra were also acquired for Au−Ag heterodimers. Measured and calculated spectra are reported for electrons incident on the edges and the center of the heterodimer (Figure S9, Supporting Information). Unlike homodimers, the primitive Au and Ag plasmon modes differ in energy, thus leading to much weaker hybridization.

CONCLUSIONS

In conclusion, we have developed a method combining NIL and shadow evaporation to pattern wafer-scale Au−Au, Ag−Ag, and Au−Ag plasmonic dimers with sub-10-nm gaps. We demonstrated gap size tuning *via* the control of the material deposition angles. The flexibility of the method allows for the dimer fabrication on a thin electron-transparent substrate such as a thin Si_3N_4 membrane, allowing TEM and EELS measurements, and can be extended to materials other than Au and Ag. An EELS-FDTD method and PH theory have been employed to interpret the EELS measurements and revealed the complex surface plasmon mode configuration in the current symmetry-broken nanostructures.

The ability to pattern wafer-scale dimers with very small gap-to-diameter ratios is crucial for practical applications. Thanks to the extremely large local-field enhancements generated within the sub-10-nm gaps consistently patterned throughout the surface, the substrate can be used in surface-enhanced spectroscopies, as well as in bio- and molecular sensing. The approach can also be used to tailor substrates for fundamental studies such as plasmon hybridization, second-harmonic generation, plasmon-exciton

and plasmon-molecule coupling, and nonlocal effects. However, these aspects are beyond the scope of the present work and will be the focus of future work.

METHODS

Patterning of Dimer Structure. After the substrate (either Si wafer or Si_3N_4 membrane on a Si wafer) was cleaned by UV irradiation, it was sequentially spin-coated with PMGI (SF3, MicroChem, 3000 rpm, postbake at 200 °C) and PMMA (75k200, MicroResist-Technology, 6000 rpm, postbake at 140 °C). A self-assembled stamp with pillar structure (~150 nm in diameter, 390 nm pitch size) was then used to nanoimprint a hole pattern in the PMMA layer (180 °C, 40 bar, 60 s). After that, the wafer was dry-etched with O_2 (100 mTorr, 20 sccm, ~15 s) to remove the residue PMMA layer, followed by wet-etching using the developer (MF26A, Shipley, tetramethylammonium hydroxide based, 15 s) to form the undercut structure. The evaporation process was divided into two runs. In the first run, a pure Au or Ag source was e-beam evaporated onto the Si wafer at an angle α with respect to the normal axis of the wafer. Then, the wafer was rotated by 180° around its normal axis, and another pure Au or Ag source was evaporated at an angle β. The evaporation directions in the first and second runs and the normal axis of the wafer stayed within the same plane. The evaporation film thickness was chosen such that a 30−40 nm thickness could be reached if the evaporation direction was normal to the wafer plane. After film evaporation, a lift-off process was conducted with acetone to dissolve the PMMA layer and MF26A to dissolve the PMGI layer. Now the continuous metal sheet had peeled off and only dimer structures stayed attached atop the Si wafer.

Preparing the Dimer Sample on a Thin Si_3N_4 Membrane. As shown in Figure 3A, the TEM sample preparation process was divided into five steps. Here, double-side polished (100) Si wafers with a thickness of ~250 μm were used. In step 1, ~50 nm low-stress silicon nitride layers were coated onto both sides of the wafer through chemical vapor deposition (CVD). In step 2, a Ag−Ag, Au−Au, or Ag−Au dimer array was patterned onto one side of the wafer following the same protocol described earlier. In step 3, photoresist (Shipley 3612) was spin-coated onto the other side of the wafer (5500 rpm, 30 s, baked at 90 °C) with a thickness of ~1 μm, followed by exposure using a transparency mask of a 0.5 × 0.5 mm^2 square window array with 1.5 mm pitch size (Carl-Suss, 365 nm incident light, 10 s exposure, soft-contact). The wafer was then hard-baked at 115 °C for 1 min followed by developing using MF26A for 2 min. After rinsing with distilled water, the 0.5 × 0.5 mm^2 square window array appeared on the photoresist layer, where the underneath silicon nitride layer was exposed. In step 4, using the patterned photoresist as the mask, the exposed silicon nitride layer was dry-etched by a gas mixture of SF_6 and O_2 (500 W, SF_6 100 sccm, O_2 10 sccm), and the etching time was adjusted to be long enough to ensure the exposure of the Si layer. After the exposure of the Si surface, the photoresist was removed using acetone. Then in step 5, the Si wafer was mounted onto a special Teflon wafer holder, where the wafer side with dimer feature was protected from the KOH solution when the wafer holder was dipped into the etchant. The KOH concentration was 30%, and the temperature was set to ~90 °C. Under this condition, the exposed Si was etched at a rate of 1 μm/min. Five hours was then necessary to etch through the Si wafer and expose the silicon nitride window where dimers were patterned on the other side.

A piece of the sample with a silicon nitride square window was loaded into the TEM (FEI Tecnai G2 F20 X-TWIN) for morphology characterization. EELS experiments were performed in STEM mode using an FEI 80−300 Cs (image) corrected environmental Titan operated at 300 kV. It was equipped with a monochromator and a Tridiem 866 EEL spectrometer (Gatan Inc.). A C3 aperture of 50 μm, spectrometer entrance aperture of 2.5 mm, and camera length of 38 mm were used in the STEM-EELS data acquisition. This corresponded to a convergence semiangle of 8.4 mrad and a collection semiangle of 18.3 mrad, respectively. The energy resolution is 0.15 eV, as determined from the full-width at half-maximum of the zero-loss peak (Figure S6, Supporting Information). The area covering an entire dimer was scanned, with a typical areal size of 200 × 200 nm^2. The EEL spectrum was mapped out over the entire area, with a pixel size of 5 × 5 nm^2. After measurement, data processing was conducted to subtract the zero-loss peak using the reflected-tail model.

Numerical Simulation of EELS Measurement. We used the commercial package Lumerical FDTD Solutions to solve Maxwell's equations using the FDTD method. In the case of EELS-FDTD simulations, electric dipoles are placed along the electron beam trajectory (here taken as the *z*-axis). The electric field induced by these electric dipoles is then calculated along the *z*-axis and used to compute the EELS spectrum at each electron beam impact position. The complete description of this EELS-FDTD implementation along with the detailed numerical protocol and the mathematical formalism can be found in ref 45.

Dielectric permittivities tabulated by Johnson and Christy[49] and by Palik[50] were used for gold and silver, respectively. A constant refractive index of 2 was used for the 50 nm thick silicon nitride substrate.[51] The geometrical and size parameters of the dimers were extracted from the HAADF and SEM images. The systems are modeled as dimers consisting of two flat hemiellipsoidal nanoparticles with long axes L_1 and L_2, short axes l_1 and l_2, and height h = 40 nm. The two nanoparticles are separated by a nominal gap g = 5 nm (Figure S10, Supporting Information).

In the EELS-FDTD simulations presented here (Figure 4 and Figure S9, Supporting Information), the size parameters are taken as $(L_1/l_1, L_2/l_2)$ = (190/150, 170/130) nm for the Au−Au dimer, $(L_1/l_1, L_2/l_2)$ = (160/130, 155/110) nm for the Ag−Ag dimer, and $(L_{Au}/l_{Au}, L_{Ag}/l_{Ag})$ = (175/100, 175/110) nm for the Au−Ag dimer. To account for the small geometrical features (*e.g.*, small gap), an FDTD mesh grid of 1.5 nm was used to discretize the nanostructure. The dimensions of the FDTD simulation domain are set to 1.5 × 1.5 × 1 μm^3.

More specifically for EELS-FDTD calculations, the electric dipole is displaced with a 2 nm step along the *z*-axis. EELS-FDTD calculations were performed for electrons impacting on both the edge parts (*i.e.*, dimer ends) and the center part (*i.e.*, dimer gap) for each dimer, as performed experimentally (insets of Figure 4). The electron velocity was fixed at 0.78*c*, corresponding to a kinetic energy of 300 keV.

Conflict of Interest: The authors declare no competing financial interest.

Supporting Information Available: Angular deposition; AFM imaging of dimer sample; high-magnification TEM images; ZLP for EELS measurement; additional EELS measurements of Ag−Ag, Au−Au, and Au−Ag dimers; FDTD geometry; plasmon hybridization of Ag−Ag nanospheres dimer. The Supporting Information is available free of charge on the ACS Publications website at DOI: 10.1021/acsnano.5b03090.

Acknowledgment. This work was supported by the Center for Cancer Nanotechnology Excellence (U54CA151459), Innovative Molecular Analysis Technologies (R33CA138330) of the National Cancer Institute, the Developmental Cancer Research Award from Stanford Cancer Center (PTA 1109905-511-PABBO), the Robert A. Welch Foundation (C-1222), the Cyberinfrastructure for Computational Research funded by NSF grant CNS-0821727, and the Data Analysis and Visualization Cyberinfrastructure under NSF grant OCI-0959097. Part of this work was performed at the Stanford Nanofabrication Facility and the Stanford Nano Shared Facilities. A.M. acknowledges support from the Welch Foundation under the J. Evans Attwell-Welch Fellowship for Nanoscale Research, administrated by the

Richard E. Smalley Institute for Nanoscale Science and Technology (grant L-C-004). P.N. acknowledges support from the Army Research Office (W911NF-12-1-0407). M.Z. carried out the sample fabrication and experimental characterization. N.L., Y.C., and A.M. performed the theoretical calculations. A.L.K. performed STEM-EELS experiments. S.X.W. and P.N. designed the project. M.Z. and N.L. wrote the manuscript. All the authors discussed the results and contributed to the manuscript edits.

REFERENCES AND NOTES

1. Wang, L.; Zhu, Y.; Xu, L.; Chen, W.; Kuang, H.; Liu, L.; Agarwal, A.; Xu, C.; Kotov, N. A. Side-by-Side and End-to-End Gold Nanorod Assemblies for Environmental Toxin Sensing. *Angew. Chem., Int. Ed.* **2010**, *49*, 5472–5475.
2. Liu, N.; Tang, M. L.; Hentschel, M.; Giessen, H.; Alivisatos, A. P. Nanoantenna-Enhanced Gas Sensing in a Single Tailored Nanofocus. *Nat. Mater.* **2011**, *10*, 631–636.
3. Wi, J.; Barnard, E. S.; Wilson, R. J.; Zhang, M.; Tang, M.; Brongersma, M. L.; Wang, S. X. Sombrero-Shaped Plasmonic Nanoparticles with Molecular-Level Sensitivity and Multifunctionality. *ACS Nano* **2011**, *5*, 6449–6457.
4. Kildishev, A. V.; Boltasseva, A.; Shalaev, V. M. Planar Photonics with Metasurfaces. *Science* **2013**, *339*, 1232009.
5. Shegai, T.; Chen, S.; Miljković, V. D.; Zengin, G.; Johansson, P.; Käll, M. A Bimetallic Nanoantenna for Directional Colour Routing. *Nat. Commun.* **2011**, *2*, 481.
6. Zhao, Y.; Belkin, M. A.; Alù, A. Twisted Optical Metamaterials for Planarized Ultrathin Broadband Circular Polarizers. *Nat. Commun.* **2012**, *3*, 870.
7. Cai, Y.; Cao, Y.; Nordlander, P.; Cremer, P. S. Fabrication of Split-Rings *via* Stretchable Colloidal Lithography. *ACS Photonics* **2014**, *1*, 127–134.
8. Qin, L.; Zou, S.; Xue, C.; Atkinson, A.; Schatz, G. C.; Mirkin, C. A. Designing, Fabricating, and Imaging Raman Hot Spots. *Proc. Natl. Acad. Sci. U. S. A.* **2006**, *103*, 13300–13303.
9. Hao, E.; Schatz, G.C. Electromagnetic Fields around Silver Nanoparticles and Dimers. *J. Chem. Phys.* **2004**, *120*, 357–366.
10. Alexander, K. D.; Hampton, M. J.; Zhang, S.; Dhawan, A.; Xu, H.; Lopez, R. A High-Throughput Method for Controlled Hot-Spot Fabrication in SERS-Active Gold Nanoparticle Dimer Arrays. *J. Raman Spectrosc.* **2009**, *40*, 2171–2175.
11. Talley, C. E.; Jackson, J. B.; Oubre, C.; Grady, N. K.; Hollars, C. W.; Lane, S. M.; Huser, T. R.; Nordlander, P.; Halas, N. J. Surface-Enhanced Raman Scattering from Individual Au Nanoparticles and Nanoparticle Dimer Substrates. *Nano Lett.* **2005**, *5*, 1569–1574.
12. Nagasawa, F.; Takase, M.; Murakoshi, K. Raman Enhancement *via* Polariton States Produced by Strong Coupling between a Localized Surface Plasmon and Dye Excitons at Metal Nanogaps. *J. Phys. Chem. Lett.* **2014**, *5*, 14–19.
13. Cheng, Y.; Wang, M.; Borghs, G.; Chen, H. Gold Nanoparticle Dimers for Plasmon Sensing. *Langmuir* **2011**, *27*, 7884–7891.
14. Aćimović, S. S.; Kreuzer, M. P.; González, M. U.; Quidant, R. Plasmon Near-Field Coupling in Metal Dimers as a Step toward Single-Molecule Sensing. *ACS Nano* **2009**, *3*, 1231–1237.
15. Large, N.; Abb, M.; Aizpurua, J.; Muskens, O. L. Photoconductively Loaded Plasmonic Nanoantenna as Building Block for Ultracompact Optical Switches. *Nano Lett.* **2010**, *10*, 1741–1746.
16. Schlather, A. E.; Large, N.; Urban, A. S.; Nordlander, P.; Halas, N. J. Near-Field Mediated Plexcitonic Coupling and Giant Rabi Splitting in Individual Metallic Dimers. *Nano Lett.* **2013**, *13*, 3281–3286.
17. Manjavacas, A.; García de Abajo, F. J.; Nordlander, P. Quantum Plexcitonics: Strongly Interacting Plasmons and Excitons. *Nano Lett.* **2011**, *11*, 2318–2323.
18. Duan, H.; Fernández-Domínguez, A. I.; Bosman, M.; Maier, S. A.; Yang, J. K. W. Nanoplasmonics: Classical down to the Nanometer Scale. *Nano Lett.* **2012**, *12*, 1683–1689.
19. Lee, J.; You, M.; Kim, G.; Nam, J. Plasmonic Nanosnowmen with a Conductive Junction as Highly Tunable Nanoantenna Structures and Sensitive, Quantitative and Multiplexable Surface-Enhanced Raman Scattering Probes. *Nano Lett.* **2014**, *14*, 6217–6225.
20. Su, X.; Zhang, J.; Sun, L.; Koo, T.; Chan, S.; Sundararajan, N.; Yamakawa, M.; Berlin, A. A. Composite Organic-Inorganic Nanoparticles (COINs) with Chemically Encoded Optical Signatures. *Nano Lett.* **2005**, *5*, 49–54.
21. Braun, G.; Pavel, I.; Morrill, A. R.; Seferos, D. S.; Bazan, G. C.; Reich, N. O.; Moskovits, M. Chemically Patterned Microspheres for Controlled Nanoparticle Assembly in the Construction of SERS Hot Spots. *J. Am. Chem. Soc.* **2007**, *129*, 7760–7761.
22. Koh, A. L.; Fernández-Domínguez, A. I.; McComb, D. W.; Maier, S. A.; Yang, J. K. W. High-Resolution Mapping of Electron-Beam-Excited Plasmon Modes in Lithographically Defined Gold Nanostructures. *Nano Lett.* **2011**, *11*, 1323–1330.
23. Scholl, J. A.; García-Etxarri, A.; Koh, A. L.; Dionne, J. A. Observation of Quantum Tunneling between Two Plasmonic Nanoparticles. *Nano Lett.* **2013**, *13*, 564–569.
24. Kollmann, H.; Piao, X.; Esmann, M.; Becker, S. F.; Hou, D.; Huynh, C.; Kautschor, L.; Bösker, G.; Vieker, H.; Beyer, A.; Gölzhäuser, A.; Park, N.; Vogelgesang, R.; Silies, M.; Lienau, C. Toward Plasmonics with Nanometer Precision: Nonlinear Optics of Helium-Ion Milled Gold Nanoantennas. *Nano Lett.* **2014**, *14*, 4778–4784.
25. Haynes, C. L.; McFarland, A. D.; Smith, M. T.; Hulteen, J. C.; Van Duyne, R. P. Angle-Resolved Nanosphere Lithography: Manipulation of Nanoparticle Size, Shape, and Interparticle Spacing. *J. Phys. Chem. B* **2002**, *106*, 1898–1902.
26. Nemiroski, A.; Gonidec, M.; Fox, J. M.; Jean-Remy, P.; Turnage, E.; Whitesides, G. M. Engineering Shadows to Fabricate Optical Metasurfaces. *ACS Nano* **2014**, *8*, 11061–11070.
27. Aksu, S.; Huang, M.; Artar, A.; Yanik, A. A.; Selvarasah, S.; Dokmeci, M. R.; Altug, H. Flexible Plasmonics on Unconventional and Nonplanar Substrates. *Adv. Mater.* **2011**, *23*, 4422–4430.
28. Zhang, M.; Bechstein, D. J. B.; Wilson, R. J.; Wang, S. X. Wafer-Scale Synthesis of Monodisperse Synthetic Magnetic Multilayer Nanorods. *Nano Lett.* **2014**, *14*, 333–338.
29. Hu, W.; Zhang, M.; Wilson, R. J.; Koh, A. L.; Wi, J.; Tang, M.; Sinclair, R.; Wang, S. X. Fabrication of Planar, Layered Nanoparticles Using Tri-Layer Resist Templates. *Nanotechnology* **2011**, *22*, 185302.
30. Zhang, M.; Xie, X.; Tang, M.; Criddle, C. S.; Cui, Y.; Wang, S. X. Magnetically Ultraresponsive Nanoscavengers for Next-Generation Water Purification Systems. *Nat. Commun.* **2013**, *4*, 1866.
31. Kang, M.; Xu, T.; Park, H. J.; Luo, X.; Guo, L. J. Efficiency Enhancement of Organic Solar Cells Using Transparent Plasmonic Ag Nanowire Electrodes. *Adv. Mater.* **2010**, *22*, 4378–4383.
32. Yu, Z.; Chou, S. Y. Triangular Profile Imprint Molds in Nanograting Fabrication. *Nano Lett.* **2004**, *4*, 341–344.
33. Prodan, E.; Radloff, C.; Halas, N. J.; Nordlander, P. A Hybridization Model for the Plasmon Response of Complex Nanostructures. *Science* **2003**, *302*, 419–422.
34. Nordlander, P.; Oubre, C.; Prodan, E.; Li, K.; Stockman, M. I. Plasmon Hybridization in Nanoparticle Dimers. *Nano Lett.* **2004**, *4*, 899–903.
35. Thurn-Albrecht, T.; Schotter, J.; Kästle, G. A.; Emley, N.; Shibauchi, T.; Krusin-Elbaum, L.; Guarini, K.; Black, C. T.; Tuominen, M. T.; Russell, T. P. Ultrahigh-Density Nanowire Arrays Grown in Self-Assembled Diblock Copolymer Templates. *Science* **2000**, *290*, 2126–2129.
36. Yang, X.; Wan, L.; Xiao, S.; Xu, Y.; Weller, D. K. Directed Block Copolymer Assembly *versus* Electron Beam Lithography for Bit-Patterned Media with Areal Density of 1 Terabit/inch^2 and Beyond. *ACS Nano* **2009**, *3*, 1844–1858.
37. García de Abajo, F. J. Optical Excitations in Electron Microscopy. *Rev. Mod. Phys.* **2010**, *82*, 209–275.
38. Nelayah, J.; Kociak, M.; Stéphan, O.; García de Abajo, F. J.; Tencé, M.; Henrard, L.; Taverna, D.; Pastoriza-Santos, I.;

Liz-Marzán, L. M.; Colliex, C. Mapping Surface Plasmons on a Single Metallic Nanoparticle. *Nat. Phys.* **2007**, *3*, 348–353.
39. Chu, M.; Myroshnychenko, V.; Chen, C. H.; Deng, J.; Mou, C.; García de Abajo, F. J. Probing Bright and Dark Surface-Plasmon Modes in Individual and Coupled Noble Metal Nanoparticles Using an Electron Beam. *Nano Lett.* **2009**, *9*, 399–404.
40. Barrow, S. J.; Rossouw, D.; Funston, A. M.; Botton, G. A.; Mulvaney, P. Mapping Bright and Dark Modes in Gold Nanoparticle Chains Using Electron Energy Loss Spectroscopy. *Nano Lett.* **2014**, *14*, 3799–3808.
41. Kadkhodazadeh, S.; Rosenkrantz de Lasson, J.; Beleggia, M.; Kneipp, H.; Wagner, J. B.; Kneipp, K. Scaling of the Surface Plasmon Resonance in Gold and Silver Dimers Probed by EELS. *J. Phys. Chem. C* **2014**, *118*, 5478–5485.
42. Das, P.; Chini, T. K.; Pond, J. Probing Higher Order Surface Plasmon Modes on Individual Truncated Tetrahedral Gold Nanoparticle Using Cathodoluminescence Imaging and Spectroscopy Combined with FDTD Simulations. *J. Phys. Chem. C* **2012**, *116*, 15610–15619.
43. Das, P.; Kedia, A.; Kumar, P. S.; Large, N.; Chini, T. K. Local Electron Beam Excitation and Substrate Effect on the Plasmonic Response of Single Gold Nanostars. *Nanotechnology* **2013**, *24*, 405704.
44. Chaturvedi, P.; Hsu, K. H.; Kumar, A.; Fung, K. H.; Mabon, J. C.; Fang, N. X. Imaging of Plasmonic Modes of Silver Nanoparticles Using High-Resolution Cathodoluminescence Spectroscopy. *ACS Nano* **2009**, *3*, 2965–2974.
45. Cao, Y.; Manjavacas, A.; Large, N.; Nordlander, P. Electron Energy-Loss Spectroscopy Calculation in Finite-Difference Time-Domain Package. *ACS Photonics* **2015**, *2*, 369–375.
46. Aizpurua, J.; Rivacoba, A.; Apell, S. P. Electron-Energy Losses in Hemispherical Targets. *Phys. Rev. B: Condens. Matter Mater. Phys.* **1996**, *54*, 2901–2909.
47. Rivacoba, A.; Aizpurua, J.; Zabala, N. Geometry Dependence of the Energy Losses of STEM Electrons in Small Particles. *Scanning Microsc.* **1995**, *9*, 927.
48. Kadkhodazadeh, S.; Wagner, J. B.; Joseph, V.; Kneipp, J.; Kneipp, H.; Kneipp, K. Electron Energy Loss and One- and Two-Photon Excited SERS Probing of "Hot" Plasmonic Silver Nanoaggregates. *Plasmonics* **2013**, *8*, 763–767.
49. Johnson, P. B.; Christy, R. W. Optical Constants of the Noble Metals. *Phys. Rev. B* **1972**, *6*, 4370–4379.
50. Palik, E. D. *Handbook of Optical Constants of Solids*; Academic Press: New York, 1985; Vol. 1, pp 350−357.
51. Bååk, T. Silicon Oxynitride: a Material for GRIN Optics. *Appl. Opt.* **1982**, *21*, 1069.